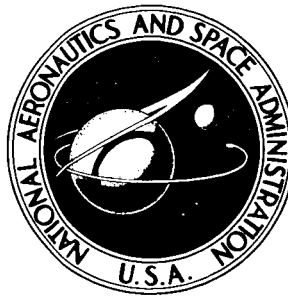


NASA TECHNICAL NOTE



NASA TN D-2848

NASA TN D-2848

N65-24383

FACILITY FORM 602

(ACCESSION NUMBER)	(THRU)
34	1
(PAGES)	(CODE)
	01
(NASA CR OR TMX OR AD NUMBER)	(CATEGORY)

# EXPERIMENTAL AERODYNAMIC CHARACTERISTICS OF 10 SHORT AXISYMMETRIC BODIES AT MACH NUMBERS OF 5 TO 15

by Gary T. Chapman, James E. Terry, and Scott Bruin

Ames Research Center  
Moffett Field, Calif.

OTS PRICE(S) \$ 3.10

Hard copy (HC) \_\_\_\_\_

Microfiche (MF) 50

EXPERIMENTAL AERODYNAMIC CHARACTERISTICS OF  
10 SHORT AXISYMMETRIC BODIES AT  
MACH NUMBERS OF 5 TO 15

By Gary T. Chapman, James E. Terry,  
and Scott Bruin

Ames Research Center  
Moffett Field, Calif.

NATIONAL AERONAUTICS AND SPACE ADMINISTRATION

---

For sale by the Clearinghouse for Federal Scientific and Technical Information  
Springfield, Virginia 22151 - Price \$2.00

EXPERIMENTAL AERODYNAMIC CHARACTERISTICS OF  
10 SHORT AXISYMMETRIC BODIES AT  
MACH NUMBERS OF 5 TO 15

By Gary T. Chapman, James E. Terry,  
and Scott Bruin  
Ames Research Center

SUMMARY

24383

The aerodynamic characteristics of three families of short axisymmetric bodies, 10 nose shapes in all, followed by a nominal one-diameter-long cylindrical afterbody are studied. The three geometric families were sharp cones, blunted cones, and ellipsoids. Variations within each family yielded four wave drag coefficients. Experimental values of drag coefficient, lift-curve slope, dynamic-stability parameter, and center of pressure are presented and compared with results from two simple theories.

The short cylindrical afterbody contributed significantly to the lift, and also produced a rearward movement of the center of pressure; this was particularly evident with the sharp-nosed-cone configurations. The aerodynamic characteristics appear to be a stronger function of nose drag coefficient than of nose geometry per se. The aerodynamic characteristics were, in general, insensitive to Mach number with the exception of the dynamic-stability parameter; low Mach number results indicated dynamic stability while high Mach number results indicated dynamic instability.

In general, modified Newtonian theory underpredicts the drag by 5 to 30 percent; furthermore, it predicts little or no contribution to lift from the afterbody at small angles of attack. A simple hybrid theory which allowed for a contribution to lift from the afterbody showed much improvement on many of the configurations but greatly overpredicted the lift on the configurations with ellipsoidal noses. It is felt that a better estimate of the zero angle-of-attack pressure distributions would improve estimates made with the simple hybrid theory.

INTRODUCTION

AUTHOR ↑

In the design of a hypersonic vehicle for a particular mission many design compromises, or - as they are often called - trade-offs, are made. Many of these compromises affect the geometry and thus the aerodynamic characteristics of the vehicle. To determine these trade-offs in the aerodynamic characteristics the designer must rely heavily upon simple theoretical results, many of which are unproven, or on expensive machine computations,

since only a relatively small amount of experimental data may be available. Furthermore, the numerical solutions are for the most part limited to small or zero angle of attack and nondissipative flow.

A recent series of free-flight experiments, designed for the purpose of obtaining shock-wave shapes, gave a body of aerodynamic data for 10 short axisymmetric bodies with systematic variation of three basic parameters - Mach number, nose drag coefficient, and nose geometry. These data provide an opportunity to examine experimentally the effect of these three basic parameters on the aerodynamic characteristics. The shock-wave characteristics and flow fields for these same bodies were presented in references 1 and 2.

The purpose of the present report is twofold: First, to present the experimental aerodynamic characteristics of this family of 10 configurations; second, to assess the applicability of two or three simple theories by comparison with these data.

#### SYMBOLS

$A$	cross-sectional area
$a_1, \dots, a_6$	constants used in equations (6)
$C_D$	drag coefficient, $\frac{\text{total drag}}{(1/2)\rho V^2 A}$
$C_{D_{\text{eff}}}$	effective drag coefficient defined by equation (3)
$C_{D_0}$	drag coefficient at zero angle of attack
$C_{L_0}, C_{Y_0}$	trim-lift and trim-side-force coefficients
$C_{L_\alpha}$	lift-curve slope, $\frac{\partial}{\partial \alpha} \left[ \frac{\text{lift}}{(1/2)\rho V^2 A} \right]$ , per rad
$C_m$	pitching-moment coefficient, $\frac{\text{pitching moment}}{(1/2)\rho V^2 A}$
$C_{m_q} + C_{m_{\dot{\alpha}}}$	damping-in-pitch derivatives, $\frac{\partial}{\partial q} (C_m) + \frac{\partial}{\partial \dot{\alpha}} (C_m)$
$C_{m_\alpha}$	pitching-moment-curve slope, $\frac{\partial}{\partial \alpha} (C_m)$ , per rad
$C_{N_\alpha}$	normal-force-curve slope, $\frac{\partial}{\partial \alpha} \left[ \frac{\text{normal force}}{(1/2)\rho V^2 A} \right]$ , per rad
$d$	cylinder diameter

G	constant in equation (1)
$I_x, I_y$	mass moment of inertia about roll and pitch axis, respectively
k	ballistic parameter, $\frac{\rho A}{2m}$
$l_{cy}$	length of cylindrical afterbody
$l_n$	length of nose section
M	free-stream Mach number
m	model mass
P	static pressure
p	roll rate
q	dimensionless pitching velocity with respect to wind-tunnel center line
R	free-stream Reynolds number, $\frac{\rho V d}{\mu}$
r	nose radius
t	time
V	free-stream velocity
X	distance from model nose along axis of model
$X_{cg}$	distance from model nose cylinder intersection to center of gravity
$X_{cp}$	distance from model nose cylinder intersection to center of pressure
x,y,z	coordinates along and orthogonal to the tunnel
$\dot{\alpha}$	dimensionless pitching velocity relative to velocity vector
$\alpha, \beta$	angles of attack and sideslip, respectively
$\alpha_r$	resultant angle of attack, $\tan^{-1} \sqrt{\tan^2 \alpha + \tan^2 \beta}$
$\alpha_{rms}$	root-mean-square resultant angle of attack
$\xi$	dummy variable
$\left. \begin{matrix} \eta_1, \eta_2 \\ \omega_1, \omega_2 \end{matrix} \right\}$	constants in equations (6)
$\theta$	cone angle

$\lambda$  wave length of pitching oscillations  
 $\mu$  coefficient of viscosity of free-stream air  
 $\xi$  dynamic-stability parameter (defined by eq. (8))  
 $\rho$  free-stream air density  
 $\sigma$  radius of gyration

#### Subscript

i initial conditions

### TEST PROCEDURE

Small-scale models were gun launched at high speeds through a counter-current supersonic flow or still air, and the position and angular orientation of the models were measured as a function of time. The aerodynamic characteristics of the models were determined from these data.

#### Models and Sabots

The models were cylinders nominally one-diameter-long with various nose geometries. The nose configurations were selected to cover a systematic variation of geometry and nose drag. The families tested - sharp cones, spherically blunted cones, and ellipsoids - are shown in figure 1. Within each family, noses were designed to have four nominal drag coefficients, 0.5, 0.9, 1.3, and 1.8, which were estimated from modified Newtonian theory ( $C_p = C_{p_{\max}} \sin^2 \theta$ ) and reference 3. The flat-faced cylinder was common to all three geometries, so there was a total of 10 different configurations. A photograph of the complete series is shown in figure 2.

The small flange at the base of each model (see fig. 2) supported a thin sheet of plastic, which prevented the remainder of the model from rubbing the gun bore. In general, this flange was about as thick as the boundary layer and, in many cases, was partially worn off from barrel friction. The wear was not always symmetric, as evidenced by the shock wave in the region of the flange. The flange is thought to have only slight effects on the aerodynamic characteristics.

#### Test Facilities and Flow Conditions

The tests were conducted in the Ames supersonic free-flight wind tunnel. Only a brief description of this facility will be given since a detailed description is given in reference 4.

The supersonic free-flight wind tunnel is an unheated blowdown supersonic wind tunnel with interchangeable nozzles giving free-stream Mach numbers of 2 or 3. The tunnel has a 27-foot-long test section through which gun-launched models are fired. There are nine observation stations at 3-foot intervals along the test section and each station is equipped with a pair of orthogonal spark shadowgraph systems for obtaining model position and orientation. The time between successive spark shadowgraphs is recorded to give the time history of the flight. Tests can be conducted either in the countercurrent air stream or through still air.

Various model velocities were used in combination with countercurrent air-stream Mach numbers of 0 and 3 to obtain nominal test Mach numbers of 5, 10, and 15. Tests without flow ( $M \approx 5$ ) were conducted at 1 atm pressure to give a nominal free-stream Reynolds number of 1.6 million based on model diameter. The free-stream static pressure of the shots with countercurrent air stream (countercurrent air stream had a Mach number of 3) was adjusted to give the same nominal Reynolds number of 1.6 million at Mach number 10. However, the minimum pressure at which the wind tunnel could be operated yielded a test Reynolds number of 2.5 million for the tests at Mach number 15. Under these conditions, the flow over the models at  $M = 5$  and 10 can be considered as a perfect gas; however, at  $M = 15$  some oxygen dissociation will occur in stagnation regions. The test conditions for each shot are given in table I.

#### DATA REDUCTION

The measured position ( $x, y, z$ ), angular orientation ( $\alpha, \beta$ ), and time ( $t$ ) data were analyzed by means of the equations of linear and angular momentum to yield the various aerodynamic characteristics. Some typical measurements giving the linear motion in three dimensions and the angular in two dimensions, for a single test, are shown in figure 3. The method of analyzing such data and the various assumptions employed will be described in the following paragraphs.

#### Drag

For a drag coefficient of the form

$$C_D = C_{D_0} + G\alpha_r^2 \quad (1)$$

where  $C_{D_0}$  is the zero angle drag coefficient,  $G$  is a constant normally taken to be the lift-curve slope, and  $\alpha_r$  is the resultant angle of attack, reference 5 shows

$$C_{D_{eff}} = \frac{1}{k} \frac{d(l_n V)}{dx} \quad (2)$$

where  $k = \rho A/2m$ ,  $d(\ln V)/d(x)$  is the slope of the plot of  $\ln(V)$  versus  $x$  (because of the small change in  $V$ , this is nearly the same as the slope of a plot of  $V$  versus  $x$  (see fig. 3(a)), and  $C_{D_{eff}}$  is given by

$$C_{D_{eff}} = C_{D_0} + C_{L_\alpha} \alpha_{rms}^2 \quad (3)$$

where

$$\alpha_{rms}^2 = \frac{1}{x} \int_0^x \alpha_r^2 d\xi$$

From equations (1) and (3) it can be seen that  $C_{D_{eff}}$  is that value of  $C_D$  which occurs at a resultant angle of attack equal to the root-mean-square resultant angle of attack.

#### Lift-Curve Slope

To determine  $C_{L_\alpha}$ , the swerve (i.e., varying translation in the directions  $y$  and  $z$ , a typical example is shown in fig. 3(b)) was analyzed by means of the linear-momentum equations (ref. 6). The motion in the two directions can be combined as a complex number and written as

$$-y'' + iz'' = \frac{\rho A}{2m} \left[ C_{L_\alpha} (\beta + i\alpha) + (-C_{Y_0} + iC_{L_0}) e^{ipx} \right] \quad (4)$$

where the double prime means differentiation twice with respect to  $x$ ;  $C_{Y_0}$  and  $C_{L_0}$  are the trim-side-force and trim-lift coefficients, respectively. Equation (4), integrated twice, yields

$$\begin{aligned} -y + iz = (-y + iz)_i + (y' + iz')_i x + \frac{\rho A}{2m} \left[ C_{L_\alpha} \int_0^x \int_0^x (\beta + i\alpha) d\xi d\zeta \right. \\ \left. + (-C_{Y_0} + iC_{L_0}) \left( \frac{1 + ipx - e^{ipx}}{p^2} \right) \right] \end{aligned} \quad (5)$$

where the subscript  $i$  refers to initial conditions. This derivation is based on the following assumptions: (1) The velocity is constant over the length of the flight; (2)  $C_{Y_0}$ ,  $C_{L_0}$ , and  $C_{L_\alpha}$  are constant; (3) lift due to angular rates is ignored; (4) the angles  $\alpha$  and  $\beta$  are small and are determined from equations for the oscillatory motion (eqs. (6a) and (6b) of next



section) which were fitted to the experimental values of  $\alpha$  and  $\beta$ . This last point will be discussed in more detail in the following section. To deduce the constants  $C_{Y_0}$ ,  $C_{L_0}$ , and  $C_{L_\alpha}$ , a differential correction procedure was used to fit equation (5) to the experimental position data by the method of least squares.

### Stability

The static- and dynamic-stability characteristics were determined by the tricyclic method of Nicolaides (ref. 6). This approach allows for constant spin and small amounts of trim. The basic assumptions are: near-perfect axial symmetry of the models, small angular displacements, linear pitching and yawing moments, and a dynamic-stability parameter that is independent of angle of attack. Under these assumptions the solutions to the angular momentum equations in pitch and yaw are

$$\alpha = e^{\eta_1 x} (a_1 \sin \omega_1 x + a_2 \cos \omega_1 x) + e^{\eta_2 x} (a_3 \sin \omega_2 x + a_4 \cos \omega_2 x) + (a_5 \sin px + a_6 \cos px) \quad (6a)$$

$$\beta = e^{\eta_1 x} (a_1 \cos \omega_1 x - a_2 \sin \omega_1 x) - e^{\eta_2 x} (a_3 \cos \omega_2 x - a_4 \sin \omega_2 x) + (a_5 \cos px - a_6 \sin px) \quad (6b)$$

To obtain the constants  $\omega_1$ ,  $\omega_2$ ,  $\eta_1$ ,  $\eta_2$ ,  $a_1$ ,  $a_2$ ,  $a_3$ ,  $a_4$ ,  $a_5$ , and  $a_6$  ( $p$  is related to  $\omega_1$  and  $\omega_2$ ), a differential correction procedure was used to fit equations (6a) and (6b) to the experimental data (e.g., fig. 3(c)) by the method of least squares.

The slope of the pitching-moment curve,  $C_{m_\alpha}$ , is related to the wave length of the pitching oscillation,  $\lambda$ , by

$$-C_{m_\alpha} = \frac{8\pi^2 I_y}{\lambda^2 \rho A d} \quad (7)$$

where  $\lambda$  is obtained from the constants  $\omega_1$  and  $\omega_2$  in equations (6a) and (6b) as

$$\lambda = \frac{2\pi}{\sqrt{\omega_1 \omega_2}} \quad (8)$$

Similarly, the dynamic-stability parameter  $\xi$  is related to the constants  $\eta_1$  and  $\eta_2$  of equations (6a) and (6b) by

$$\xi = \frac{2m}{\rho A} (\eta_1 + \eta_2) \quad (9)$$

where  $\xi$  is defined as

$$\xi = C_D - C_{L\alpha} + (C_{mq} + C_{m\dot{\alpha}})(d/\sigma)^2 \quad (10)$$

This parameter is often referred to as the constant altitude dynamic-stability parameter for unpowered flight and is discussed in more detail in reference 7.

Under the assumptions governing equations (6) the values of  $C_{m\alpha}$  and  $\xi$  obtained from this technique are constants representing a linear dynamic system. Nonlinearities that may exist in the characteristics of the models being tested are thus represented by values of  $C_{m\alpha}$  and  $\xi$  which define an "equivalent linear system."

#### Center of Pressure

The center of pressure,  $X_{cp}$ , may be determined from the definition of the pitching-moment-curve slope:

$$C_{m\alpha} = \left( \frac{X_{cg}}{d} - \frac{X_{cp}}{d} \right) C_{N\alpha} \quad (11)$$

This equation, when solved for  $X_{cp}/d$ , gives

$$\frac{X_{cp}}{d} = \frac{X_{cg}}{d} - \frac{C_{m\alpha}}{C_{N\alpha}} \quad (12)$$

where for small angles of attack the slope of the normal-force curve,  $C_{N\alpha}$ , is given by

$$C_{N\alpha} = C_D + C_{L\alpha} \quad (13)$$

#### Error Analysis

The estimated accuracies of the basic measurements are

$$\begin{array}{ll} x, y, z & \pm 0.005 \text{ in.} \\ t & \pm 1.25 \text{ } \mu\text{sec} \\ \alpha, \beta & \pm 0.2^\circ \end{array}$$

The accuracy of inferred aerodynamic parameters is very difficult to determine. However, experience and repeatability indicate that  $C_D$  and  $C_{m\alpha}$  are very good (less than 5-percent error). The accuracy of  $C_{L\alpha}$ , which

depends on many factors, such as  $\alpha_r$ ,  $C_{L\alpha}$ ,  $\rho A/2m$  and the distance flown, is generally not as good. The repeatability of the present results indicates an accuracy of  $\pm 0.15$  per radian; there are a couple of cases with larger scatter. Although the accuracy of the dynamic-stability parameter  $\xi$  is generally not very good, it does determine convergence or divergence and indicates strong trends. The accuracy of the center of pressure which is derived from  $C_D$ ,  $C_{m\alpha}$ , and  $C_{L\alpha}$  lies between the accuracy of  $C_{m\alpha}$  and  $C_{L\alpha}$ .

## RESULTS AND DISCUSSION

The aerodynamic characteristics  $C_D$ ,  $C_{L\alpha}$ ,  $C_{m\alpha}$ ,  $\xi$ , and  $X_{cp}$ , experimentally determined for the family of 10 configurations at nominal Mach numbers of 5, 10, and 15, are basically for small angles of attack, but some exceptions will be noted. The experimental results along with the flight conditions are listed in table I. A discussion of these results, as well as comparisons with simple theories, where applicable, follows.

### Drag and Lift-Curve Slope

Drag.- The drag coefficients at zero angle of attack,  $C_{D_0}$ , plotted in figure 4 is the measured drag coefficient,  $C_{D_{eff}}$ , corrected for drag due to lift. This correction was made using equation (3) with measured values of  $C_{L\alpha}$  and  $\alpha_{rms}$ . In most cases the correction was small. The effect of Mach number on the drag coefficient is small in the range tested. Comparison with modified Newtonian theory is made with results from all configurations tested and comparisons with reference 3 are made for the two sharp-cone models with attached bow waves. The drag coefficient for the two sharp-cone models with higher drag could not be determined from reference 3 because their shock waves are detached.

Good agreement was obtained between the test results and the drag coefficients calculated by the method of reference 3 for the two cones with the lowest drag. Including skin friction and base drag would probably improve the agreement. In general, modified Newtonian theory consistently predicts low drag coefficients, varying from 5 to 30 percent. The major exception to this is the drag coefficient of the flat-faced configuration which was over-predicted because the modified Newtonian theory failed to account for pressure decreasing to the sonic condition at the corner.

Lift-curve slope.- The experimental lift-curve slope results are plotted in figure 5 as a function of free-stream Mach number. The scatter in these data is larger than in the drag data, as was discussed in the error analysis section. However, because of their internal consistency, the present results are considered to be good. The lift-curve slope appears to be constant or to decrease slightly with Mach number, but the scatter makes it difficult to say which of these is correct.

Comparison with modified Newtonian theory shows poor agreement. This is not too surprising when one considers that this theory accounts for no contribution to the lift curve on the cylindrical afterbody at zero angle of attack. Note the curve for the flat-faced body is not shown; it is  $C_{L\alpha} \approx -1.8$  and would fall well below the data.

A comparison is also made with a simple hybrid theory which includes a contribution to lift, at small angles of attack, from the afterbody. This hybrid theory uses modified Newtonian or reference 3 calculations on the nose and a local perturbation theory (ref. 8) on the afterbody. The local perturbation theory is basically as follows: Given a zero angle-of-attack pressure distribution, expand the flow locally on the leeward meridian and isentropically compress the flow locally on the windward meridian through a Prandtl-Meyer angle equal to the angle of attack; assume that the pressure perturbation is distributed in a cosine variation around the body; finally, integrate the perturbed flow field to obtain the lift. The pressure distributions at zero angle of attack used in the present calculations are tabulated below:

Hybrid Theory		
Configuration	Theory used on nose	Zero angle-of-attack pressure distribution used on cylinder
C-0.5	Ref. 3	Constant $P/P_\infty$
C-0.9	Ref. 3	Constant $P/P_\infty$
C-1.3	Mod. Newtonian	Constant $P/P_\infty$
SC-0.5	↓	SP - Correlation equation (14)
SC-0.9		SP - Correlation equation (14)
SC-1.3		SP - Correlation equation (14)
E-0.5		Correlation equation (14)
E-0.9		Correlation equation (14)
E-1.3		Correlation equation (14)

The pressure on the forebodies was determined from reference 3, when possible, and by modified Newtonian, otherwise. The pressure just downstream of the shoulder (to be indicated by SP) on models with sharp corners was obtained using a Prandtl-Meyer equation around the corners. The pressure on the cylinder of the sharp-nosed cones was assumed to be constant and equal to the shoulder pressure, SP (this assumption of constant pressure is a simple approximation which should be fairly good for the short cylinders). For the blunted cones, a modified blast-wave-type pressure-ratio correlation equation (eq. (14)) was faired into the pressure just downstream of the shoulder (indicated in the tabulation by SP - correlation eq. (14)). For the ellipsoidal configurations, the following modified blast-wave-type correlation equation was used (indicated in the tabulation as correlation eq. (14)):

$$\frac{P}{P_\infty} = 0.024 \left( \frac{M_\infty^2 C_D^{1/2}}{x/d} \right)^{0.7} \quad (14)$$

This equation was obtained by fairing a curve through the correlated results of reference 2, with only the data for positions near the nose considered. The equation obtained is most representative of the Mach number 10 data, being too high at the lower Mach number and too low at the higher Mach number.

The comparison with the simple hybrid theory is shown in figure 5. Although there is some improvement over modified Newtonian theory, there is still much to be desired, particularly for the cases with ellipsoidal noses. For those cases which used equation (14) as all or part of the zero angle-of-attack pressure distribution the simple hybrid theory appears to overestimate the Mach number effect as a result of the pressure-correlation curve being too high at the low Mach numbers and too low at the high Mach numbers, as described earlier.

It should be noted that the accuracy of this simple hybrid theory, among other things, is a strong function of the pressure distribution used. Therefore the order of approximation of the pressure distribution is important. The pressure distribution in the first diameter or two behind the nose is very sensitive to nose geometry and Mach number. More accurate pressure distributions would, it is believed, improve the agreement, bringing it more in line with the trend exhibited by the experimental results because, as was noted above, the correlation curve used tends to overpredict the pressures at Mach number 5 and underpredict the pressures at Mach number 15.

Correlation of lift-curve slope and drag.- The experimental lift-curve slope is plotted versus the drag coefficient in figure 6 for a nominal Mach number of 10. There are three apparent advantages to this type of plot: (1) a quick comparison of various geometries can be easily made; (2) a quick over-all assessment of theory can be made; and (3) a simple approximate trade-off between lift and drag is easily obtained.

In comparing the experimental data for the various geometries, at a constant  $C_{D_0}$ , we can see that, in general, the configurations with a discontinuous slope at the nose-cylinder junction have more lift than the ellipsoidal nose configuration. Note, however, that at the high drag coefficient end of the curves all of the curves have to meet at a common point (i.e., the flat-faced cylinder is common to all the families). As  $C_{D_0}$  is increased from its lower values the lift contribution from the afterbody of the sharp-nosed configuration at first appears to increase. This can be seen from a comparison of the theory for the cone alone (considered to be a good representation of cone data) and the cone-cylinder data. However, with the change in the surface flow ahead of the shoulder from supersonic to subsonic, the lift from the afterbody decreases with further increase in  $C_p$ . This change of afterbody lift with changing  $C_p$  appears to be present in the blunt-cone data also. The changes in lift produced by the afterbody would appear to correlate with the pressure just downstream of the shoulder, particularly for the sharp cone.

Three theoretical approaches have been used to generate curves for comparison with the experimental results: the modified Newtonian and hybrid

theories for the complete configuration, and reference 3 for conical noses alone. It is interesting to note the modified Newtonian does not distinguish between configurations having the same drag. Furthermore, note that, in general, the simple hybrid theory which has a contribution to the lift-curve slope from the afterbody does provide significant improvement over the modified Newtonian theory and reference 3 for both sharp- and blunt-nosed configurations. Note the curve for the sharp-nosed cones is terminated at a  $C_D$  of about 1.2 since a theoretical calculation of  $C_D$ , based on reference 3, for the  $58^\circ$  cone is not possible because of shock detachment. The improved agreement with experimental data obtained with the simple hybrid theory over that which considers contributions from the nose only indicates the significant contribution of lift from the short cylinder. A short-curve second-order shock-expansion theory for slender bodies (ref. 9) is also shown in figure 6 for comparison with the simple hybrid theory on the cone-cylinder configurations. The two theories appear to give consistent results for the small angle cones.

The agreement between the configurations with the ellipsoidal noses and the simple hybrid theory is poor. This may be because of poor estimates of the zero angle-of-attack pressure distribution.

The trade-off between lift and drag is readily apparent in figure 6. A simple rule of thumb for this trade-off is

$$\Delta C_{L_\alpha} = -2 \Delta C_{D_0}$$

where the  $\Delta C_{L_\alpha}$  is the incremental change in lift-curve slope accompanying an incremental change  $\Delta C_{D_0}$  in drag.

#### Static Stability and Center of Pressure

Static stability.- The experimentally determined values of the static stability  $C_{m_\alpha}$  are tabulated in table I. It is not meaningful to make direct comparison of these data because the centers of gravity are different for different models. It should be noted, however, that there is a slight Mach number effect on  $C_{m_\alpha}$ . Increasing Mach number decreases  $C_{m_\alpha}$ . A better comparison of the different configurations can be made on the basis of the center-of-pressure locations obtained from  $C_{m_\alpha}$ ,  $C_{L_\alpha}$ , and  $C_D$ .

Center of pressure.- The center of pressure in diameters from the shoulder is shown plotted in figure 7 as a function of Mach number. With the exception of one or two data points, the results are internally very consistent. Also shown in this figure are the centers of pressure calculated by modified Newtonian theory and the simple hybrid theory.

The center-of-pressure position is nearly independent of Mach number, moving only slightly forward with increasing Mach number, and is highly dependent on the nose-drag coefficient, moving farther behind the shoulder

with increasing nose drag. The geometry of the nose has only a slight effect on the center-of-pressure location for configurations with the discontinuous slope at the shoulder (i.e., the sharp- and blunt-nosed cone configurations). This again appears to indicate the strong effect of the slope discontinuity on the afterbody pressure distribution. On the other hand, the ellipsoidal-nosed configurations with  $C_D = 0.5$  and  $0.9$  had a pronounced effect on the center of pressure, moving it forward.

In comparing the data with the theoretical results one can see a marked improvement in the simple hybrid theory over the modified Newtonian theory, again indicating the important contribution of the afterbody. The agreement with the simple hybrid theory is, in general, very good.

### Dynamic Stability

The present set of tests was not specifically designed for obtaining dynamic-stability data. As a result, in many of the tests the number of cycles of pitching and yawing motion observed was insufficient for obtaining accurate dynamic-stability data. Dynamic-stability data were obtained, however, in the course of analysis of the flights and are tabulated in table I, along with the number of observed cycles of motion and a notation characterizing the oscillatory motion as planar (P) or nonplanar (NP). (Whether the motion is planar or not has an effect on the apparent dynamic stability (ref. 10). This peculiarity can result from nonlinear damping.)

Bearing in mind the above limitations, we plot the dynamic-stability parameter,  $\xi$ , for those tests with one or more cycles of observed planar motion (fig. 8). Note that one cycle of observed motion is by no means sufficient for good precision. The results do, however, indicate a couple of points: First, in general, there does not appear to be any dominant effect of nose geometry or drag coefficient; and second, there appears to be a decrease in dynamic stability with increasing Mach number, the low Mach number results indicating dynamic stability and the higher Mach number results, dynamic instability.

### CONCLUDING REMARKS

The aerodynamic characteristics of three families of bodies, 10 configurations in all, at nominal Mach numbers of 5, 10, and 15, have been experimentally determined and compared with some simple theories. The following are some general observations about the results and the comparison with theory.

The short afterbody was found to contribute significantly to the lift and also to produce a rearward movement of the center of pressure; this was particularly evident for the sharp-nosed cone configuration.

Furthermore, the lift-curve slope,  $C_{L_\alpha}$ , and center of pressure appeared to be more a function of nose drag coefficient than of nose shape per se; increasing nose drag coefficient decreased  $C_{L_\alpha}$  and moved the center of pressure rearward.

The dynamic behavior appeared to change from stable at the lower Mach numbers to unstable at the higher Mach numbers.

In general, modified Newtonian theory underpredicted the drag by 5 to 30 percent and predicted little or no lift contribution from the cylindrical afterbody at small angles of attack. A simple hybrid theory which allowed for lift from the afterbody was, in general, an improvement over the modified Newtonian theory but it left much to be desired; in particular, it overpredicted the lift on the afterbody of the ellipsoidal-nosed configurations. Better estimates of the pressure distribution at zero angle of attack would probably improve the predictions made with the simple hybrid theory.

Ames Research Center

National Aeronautics and Space Administration

Moffett Field, Calif., Mar. 1, 1965



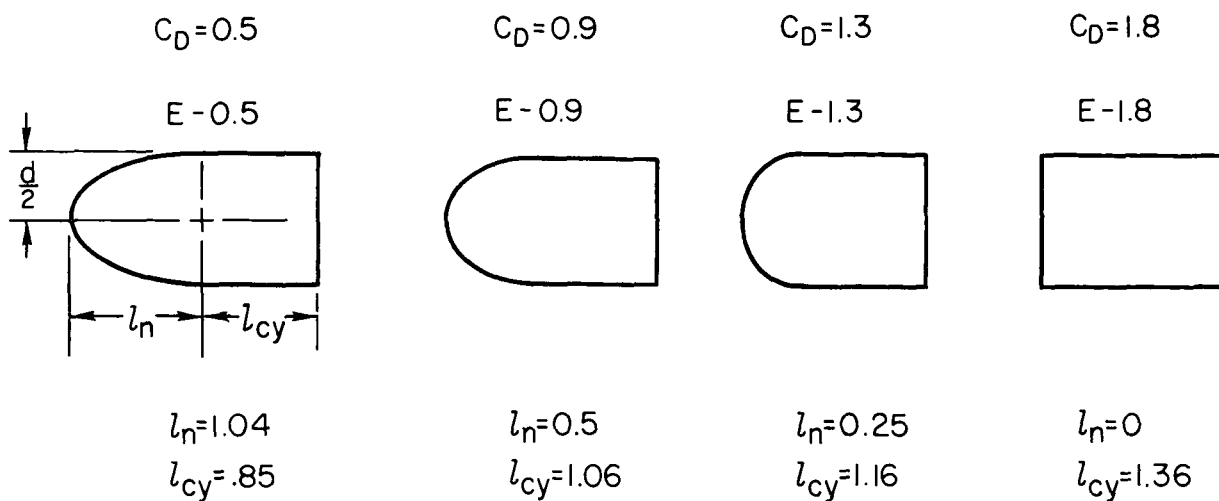
## REFERENCES

1. James, Carlton S.; and Terry, James E.: Shock-Wave Profiles Over Ellipsoidal-Nosed Bodies in Hypersonic Flow. J. Aerospace Sci., vol. 29, no. 9, Sept. 1962, pp. 1128-1129.
2. Terry, James E.; and James, Carlton S.: A Parametric Study of Hypersonic Flow Fields About Blunt-Nosed Cylinders at Zero Angle of Attack. NASA TN D-2342, 1964.
3. Staff of Computing Section, Center of Analysis (under the direction of Zdeněk Kopal): Tables of Supersonic Flow Around Yawing Cones. Tech. Rep. 3, M.I.T. Dept. of Elect. Engr., Cambridge, 1947.
4. Seiff, Alvin: A Free-Flight Wind Tunnel for Aerodynamic Testing at Hypersonic Speeds. NACA Rep. 1222, 1955.
5. Seiff, Alvin; and Wilkins, Max E.: Experimental Investigation of a Hypersonic Glider Configuration at a Mach Number of 6 and at Full-Scale Reynolds Numbers. NASA TN D-341, 1961.
6. Nicolaides, John D.: On the Free Flight Motion of Missiles Having Slight Configurational Asymmetries. BRL Rep. 858, Aberdeen Proving Ground, 1953.
7. Seiff, Alvin; Sommer, Simon C.; and Canning, Thomas N.: Some Experiments at High Supersonic Speeds on the Aerodynamic and Boundary-Layer Transition Characteristics of High-Drag Bodies of Revolution. NACA RM A56IO5, 1957.
8. Seiff, Alvin: Atmosphere Entry Problems of Manned Interplanetary Flight. Paper presented at AIAA National Meeting on Manned Interplanetary Exploration, Palo Alto, Calif., Sept. 30 and Oct. 1, 1963.
9. Syvertson, Clarence A.; and Dennis, David H.: A Second-Order Shock-Expansion Method Applicable to Bodies of Revolution Near Zero Lift. NACA TR 1328, 1957.
10. Murphy, Charles H.: An Erroneous Concept Concerning Nonlinear Aerodynamic Damping. AIAA J. vol. 1, no. 6, June 1963, pp. 1418-1419.

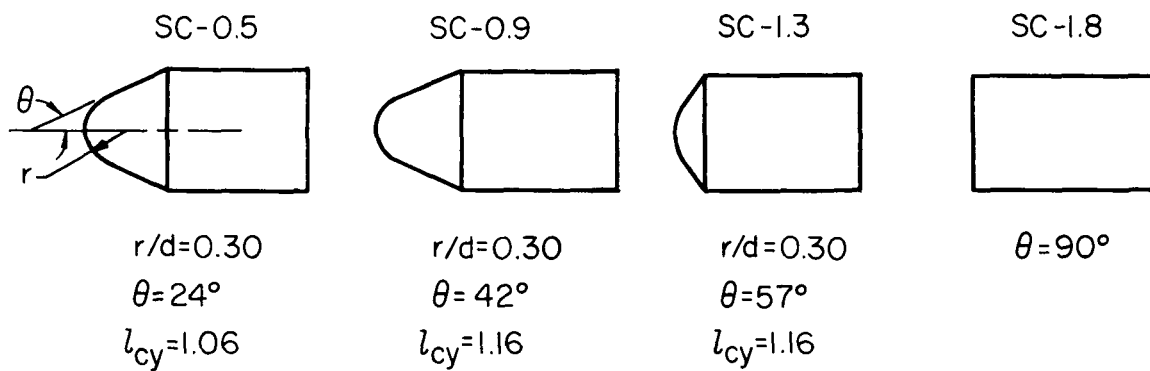
TABLE I.- TEST CONDITIONS AND TEST RESULTS

Configuration	Run	M <sub>0</sub>	R <sub>0</sub> × 10 <sup>-6</sup>	α <sub>rms</sub>	C <sub>Deff</sub>	C <sub>Lα</sub>	C <sub>mα</sub>	X <sub>cp</sub> d	ξ	l <sub>n</sub> d	X <sub>cg</sub> d	l <sub>cy</sub> d	No. of cycles and type of motion
(a) Cone-cylinders													
C-0.5	775	5.16	1.48	5.46	0.586	1.76	-0.267	0.094	-0.5	0.9020	-0.0200	1.06	1 <sup>+</sup> - NP <sup>a</sup>
C-0.5	820	5.54	1.60	8.10	.600	1.26	-.223	.094	-2.1	.9020	-.0256	1.06	1 <sup>+</sup> - P <sup>b</sup>
C-0.5	828	9.59	1.64	4.15	.546	1.27	-.149	.052	3.7	.9020	-.0306	1.06	1 <sup>+</sup> - NP
C-0.5	851	14.61	2.52	6.13	---	1.260	-.129	.045	16.9	.9020	-.0280	1.06	1/2 <sup>+</sup> - P
C-0.5	776	14.74	2.55	3.90	.558	---	-.199	---	34.7	.9020	-.0340	1.06	3/4 <sup>+</sup> - P
C-0.9	821	5.27	1.56	2.56	1.09	1.22	-.441	.483	-.34	.5000	.1456	1.16	1-1/2 <sup>+</sup> - P
C-0.9	825	10.07	1.69	15.11	1.07	.789	-.296	.304	.67	.4999	.1450	1.16	1 <sup>+</sup> - P
C-0.9	855	14.80	2.48	3.95	1.08	.782	-.327	.322	4.07	.5000	.1460	1.16	1 <sup>+</sup> - NP
C-1.3	822	5.08	1.46	5.27	1.54	-.477	-.293	.503	-2.7	.3124	.2279	1.16	1-1/2 <sup>+</sup> - P
C-1.3	824	9.76	1.72	4.08	1.50	-.561	-.299	.544	-8.0	.3123	.2257	1.16	1 <sup>+</sup> - P
C-1.3	832	15.19	2.56	2.05	1.50	---	-.299	---	1.8	.3123	.2288	1.16	1 <sup>+</sup> - P
C-1.8	801	4.04	1.18	1.94	1.67	---	-.422	---	-11.0	0	-.3352	1.36	---
C-1.8	819	4.64	1.36	1.6	1.68	---	---	---	---	0	---	1.36	---
C-1.8	805	5.14	1.49	5.73	1.73	-.743	-.354	.697	-2.5	0	-.3394	1.36	1 <sup>+</sup> - P
C-1.8	914	8.32	1.37	3.83	1.70	-.742	-.332	.681	-58.7	0	-.3430	1.46	---
C-1.8	916	9.14	1.48	3.31	1.76	-.701	-.302	.636	4.0	0	-.3506	1.46	1 <sup>+</sup> - NP
C-1.8	841	9.66	1.67	7.20	1.69	-.715	-.295	.643	3.6	0	-.3389	1.36	1 <sup>+</sup> - P
C-1.8	808	9.84	1.69	9.20	1.72	---	-.278	---	-3.0	0	-.3357	1.36	1 <sup>+</sup> - NP
C-1.8	842	14.16	2.44	5.60	1.64	-1.01	-.194	.654	39.0	0	-.3388	1.36	1 <sup>+</sup> - NP
(b) Sphere-cone-cylinders													
SC-0.5	912	3.91	1.10	8.60	.664	1.35	-.333	.100	-1.9	.6851	-.0645	1.06	1 <sup>+</sup> - P <sup>b</sup>
SC-0.5	906	4.85	1.36	8.92	.583	.933	-.241	.104	-.5	.6851	-.0649	1.06	1 <sup>+</sup> - P
SC-0.5	850	5.15	1.48	10.0	.635	---	---	---	---	.6855	-.1016	1.16	---
SC-0.5	901	10.30	1.70	4.40	.497	1.07	-.173	.051	-10.3	.6853	-.0597	1.06	1 <sup>+</sup> - NP <sup>a</sup>
SC-0.5	844	10.24	2.03	15.0	.653	1.02	-.080	.150	-50.1	.6855	-.1016	1.16	1/2 <sup>+</sup> - P
SC-0.5	903	14.34	2.39	9.97	.553	1.474	-.163	.020	-36.6	.685	-.0610	1.06	1/2 <sup>+</sup> - NP
SC-0.9	849	4.92	1.40	4.84	1.04	.743	-.383	.350	-1.3	.4066	.1356	1.16	1 <sup>+</sup> - NP
SC-0.9	826	10.28	1.82	4.71	.988	.744	-.295	.306	.8	.4069	.1359	1.16	1 <sup>+</sup> - P
SC-0.9	852	15.09	2.55	6.90	.986	.635	-.283	.309	1.7	.4068	.1343	1.16	1 <sup>+</sup> - P
SC-1.3	913	4.13	1.15	2.5	1.48	-.242	-.304	.464	6.1	.2670	.2302	1.16	1 <sup>+</sup> - NP
SC-1.3	848	5.14	1.49	8.63	1.37	-.358	-.290	.518	-1.1	.2668	.2299	1.16	1 <sup>+</sup> - P
SC-1.3	827	10.52	1.79	6.30	1.46	-.368	-.318	.566	-.1	.2669	.2283	1.16	1-1/2 <sup>+</sup> - NP
SC-1.3	920	14.41	2.40	4.0	1.49	-.011	-.379	.484	-.3	.2671	.2298	1.16	1 <sup>+</sup> - NP
SC-1.3	843	15.04	2.58	9.83	1.39	-.277	-.290	.491	2.2	.2668	.2293	1.16	1 <sup>+</sup> - P
(c) Ellipsoid-cylinders													
E-0.5	905	4.54	1.28	15.40	.721	1.00	-.302	-.204	-2.1	1.0416	-.3791	.852	1 <sup>+</sup> - P <sup>b</sup>
E-0.5	902	9.75	1.63	14.47	.590	.923	-.188	-.262	-72.3	1.042	-.3770	.852	3/4 <sup>+</sup> - NP <sup>a</sup>
E-0.5	845	10.63	1.88	23.09	.725	---	-.123	---	-4.2	1.042	-.2610	.852	1/2 <sup>+</sup> - NP
E-0.5	907	12.96	2.06	17.22	.690	---	-.194	---	-4.4	1.042	-.3310	.852	1/2 <sup>+</sup> - NP
E-0.9	807	4.68	1.63	8.65	.944	---	-.249	---	5.0	.500	-.0220	1.06	3/4 <sup>+</sup> - NP
E-0.9	823	5.03	1.44	4.48	.935	.500	-.311	.206	-1.7	.5001	-.0108	1.06	1 <sup>+</sup> - P
E-0.9	802	5.51	1.63	13.1	.944	.452	-.320	.209	1.0	.500	-.0247	1.06	1 <sup>+</sup> - NP
E-0.9	839	9.56	1.62	5.51	.894	.146	-.246	.226	1.1	.5006	-.0103	1.06	1 <sup>+</sup> - P
E-0.9	856	14.41	2.40	3.57	.852	.519	-.237	1.53	11.8	.5002	-.0071	1.06	1 <sup>+</sup> - NP
E-0.9	806	14.80	2.55	9.08	.854	---	-.230	---	-3.0	.500	-.0198	1.06	1 <sup>+</sup> - NP
E-1.3	847	4.73	1.38	3.32	1.24	---	-.346	---	9.2	.2502	.1650	1.16	1 <sup>+</sup> - P
E-1.3	831	9.56	1.66	2.49	1.25	-.459	-.312	.560	1.3	.2500	.1646	1.16	1 <sup>+</sup> - P
E-1.3	853	14.81	2.46	7.83	1.29	-.246	-.294	.446	.8	.2501	.1655	1.16	1 <sup>+</sup> - P

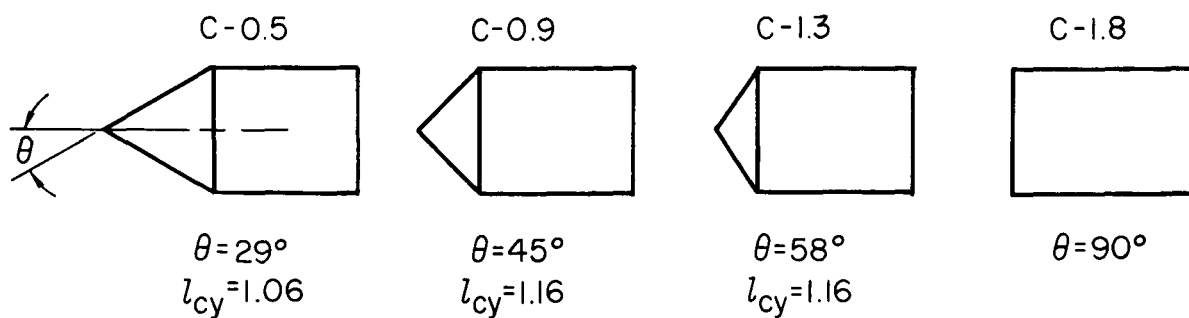
<sup>a</sup>Planar motion<sup>b</sup>Nonplanar motion



### Ellipsoid-cylinder

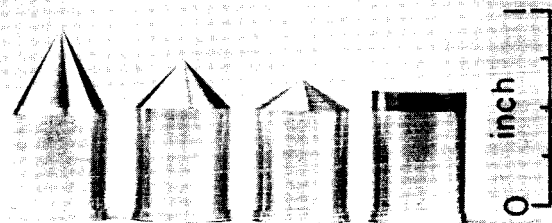


### Sphere-cone-cylinder

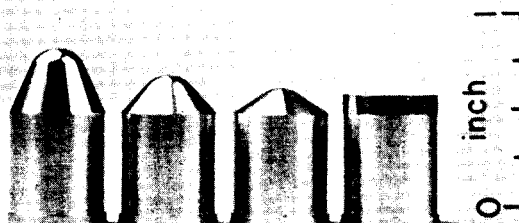


### Cone-cylinder

Figure 1.- Configurations tested.



A-27689

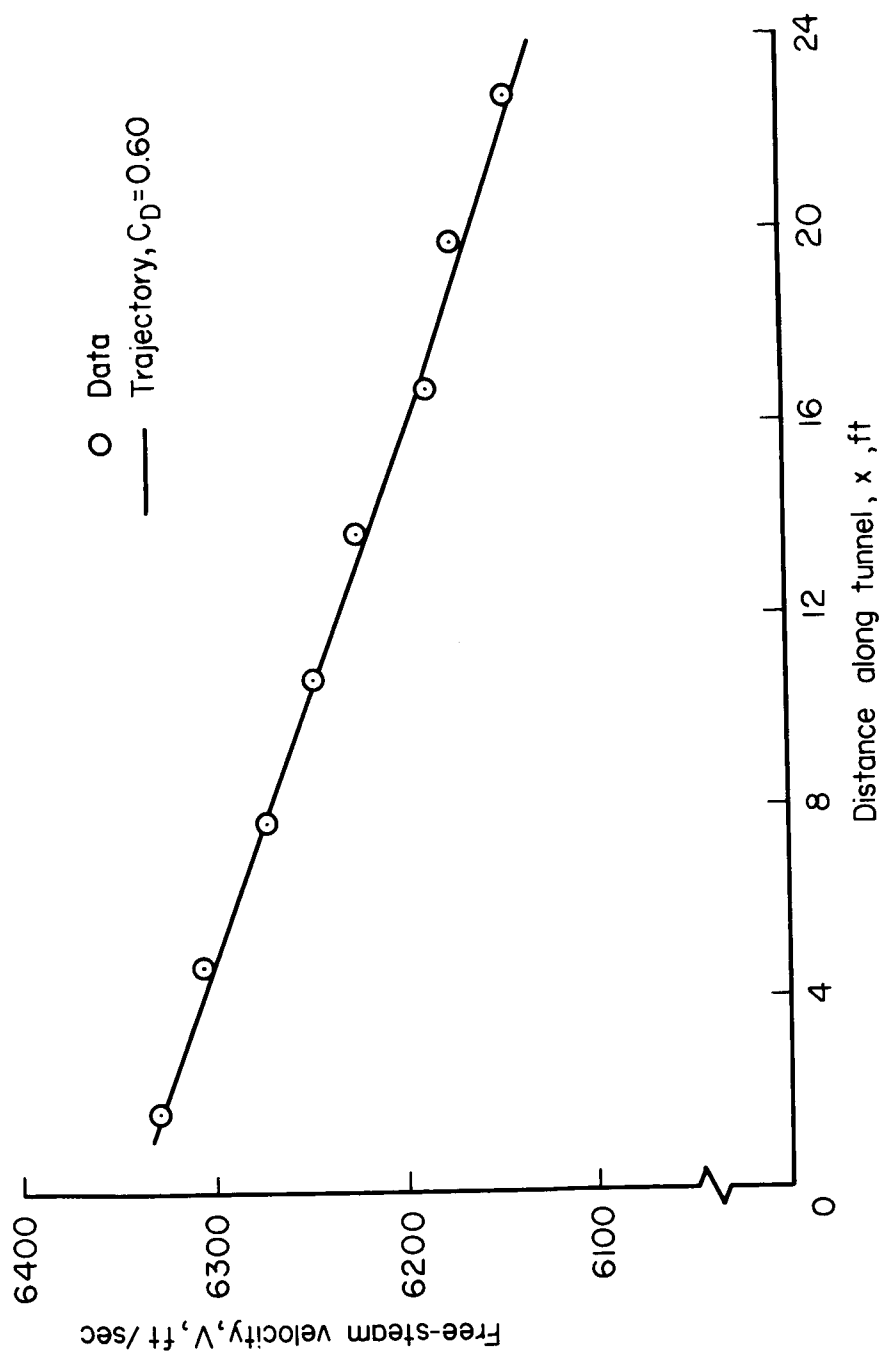


A-27690



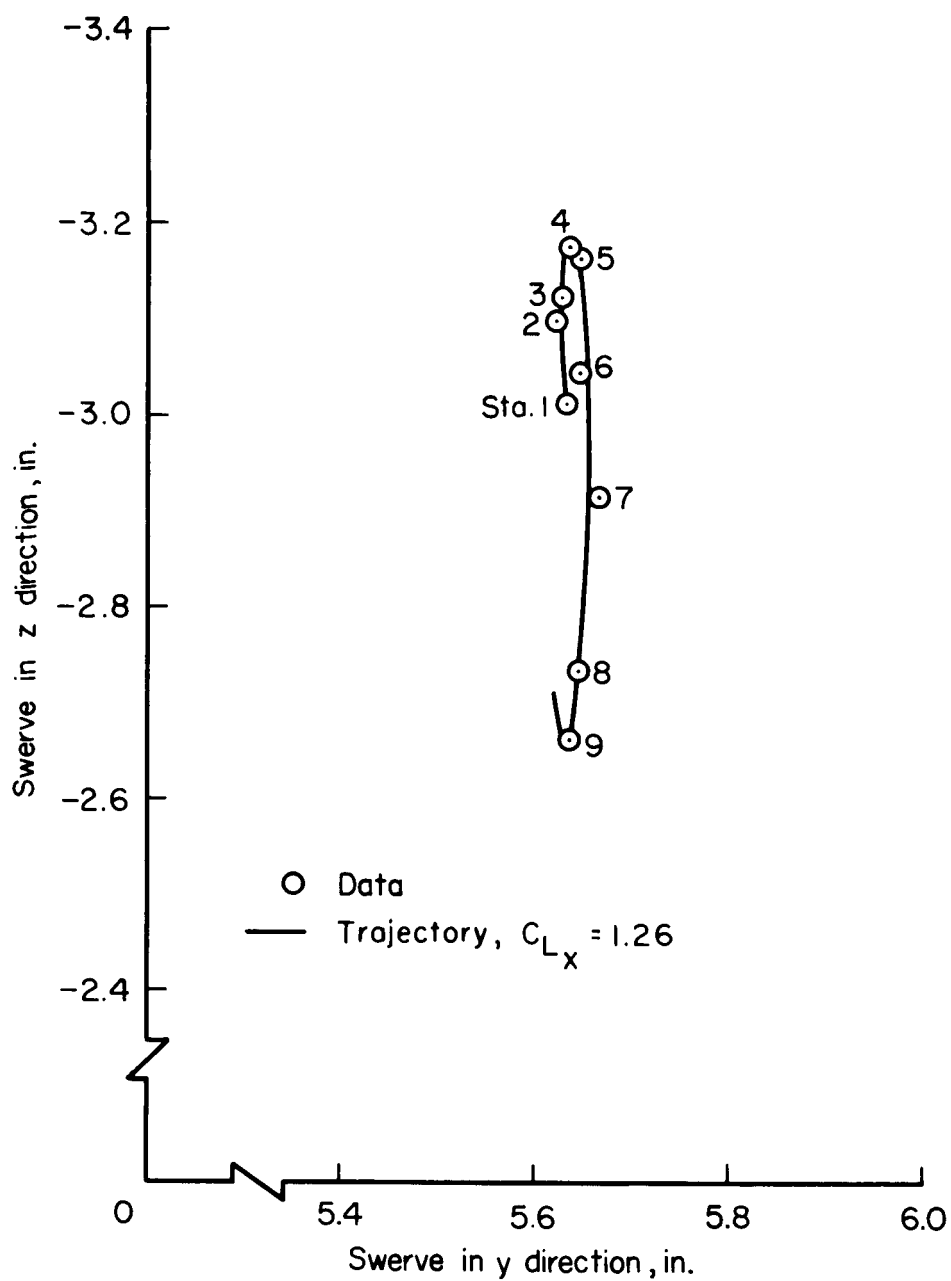
A-27691

Figure 2.- Test models.



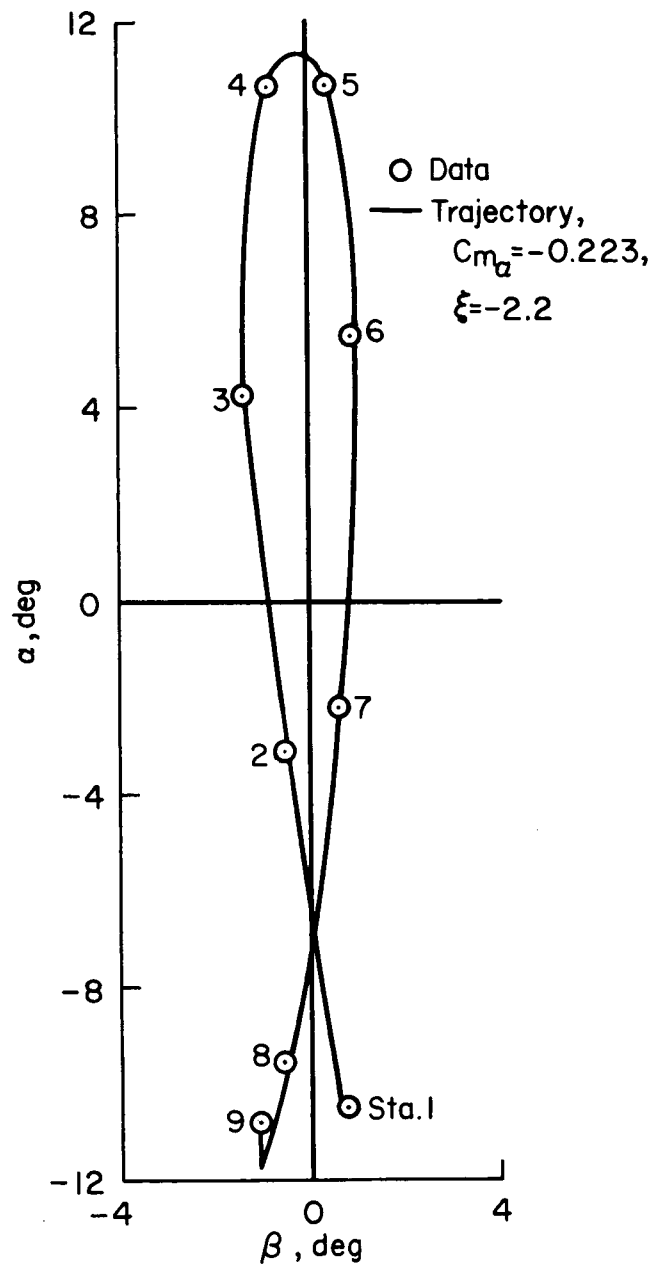
(a) Velocity history.

Figure 3.- Typical velocity, orientation, and position data.



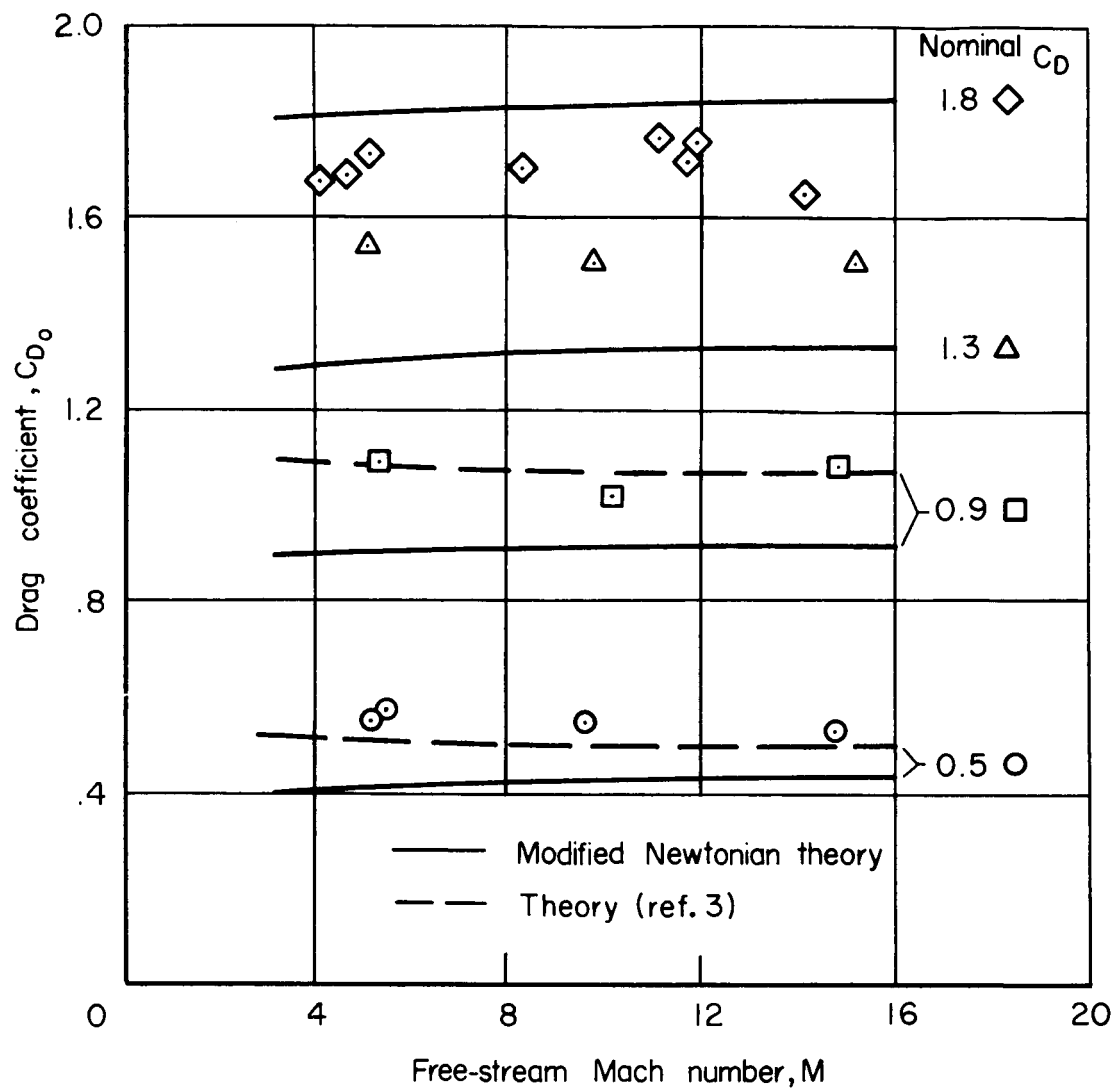
(b) Position data.

Figure 3.- Continued.



(c) Angular orientation.

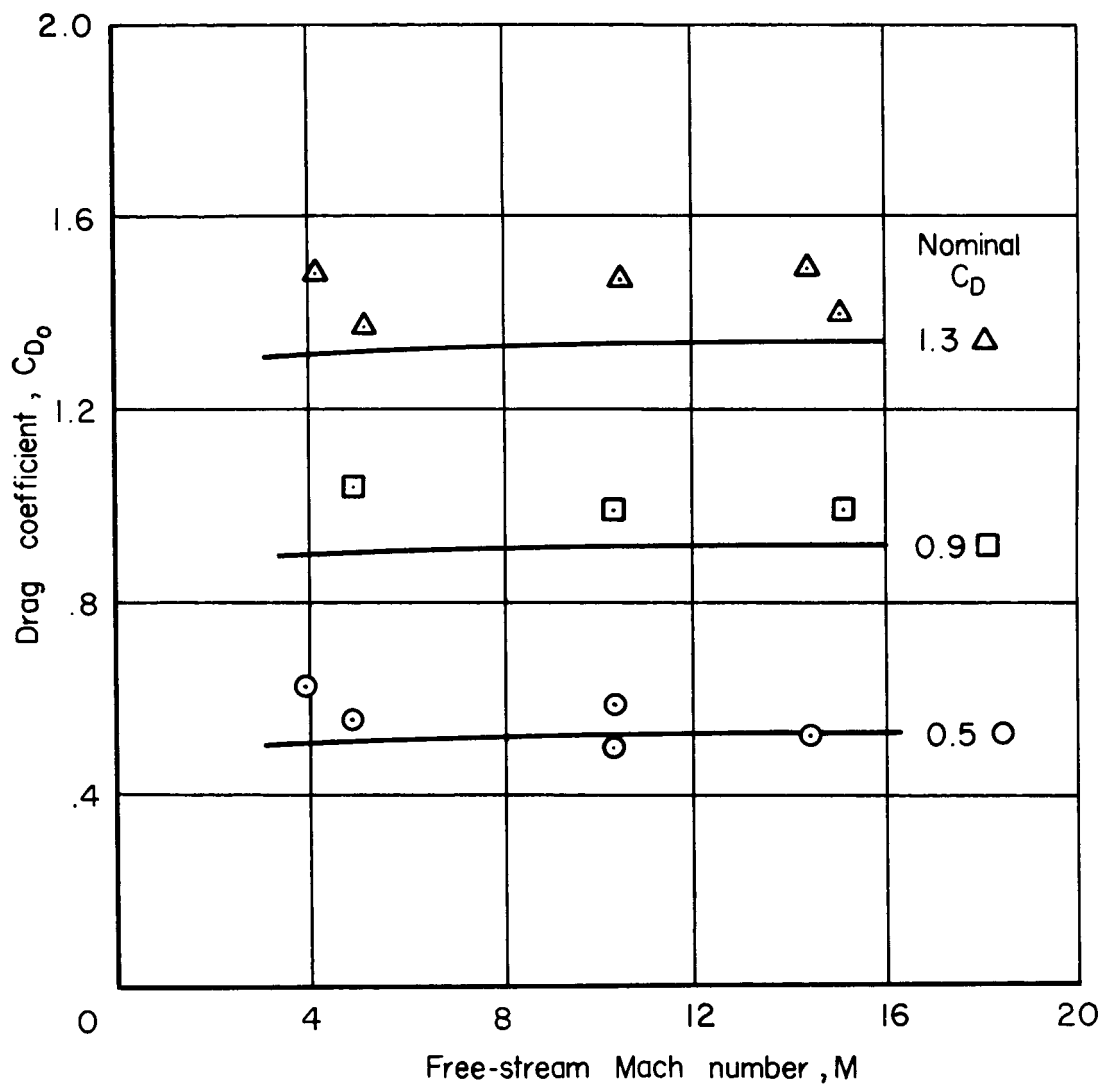
Figure 3.- Concluded.



(a) Cone-cylinder configurations.

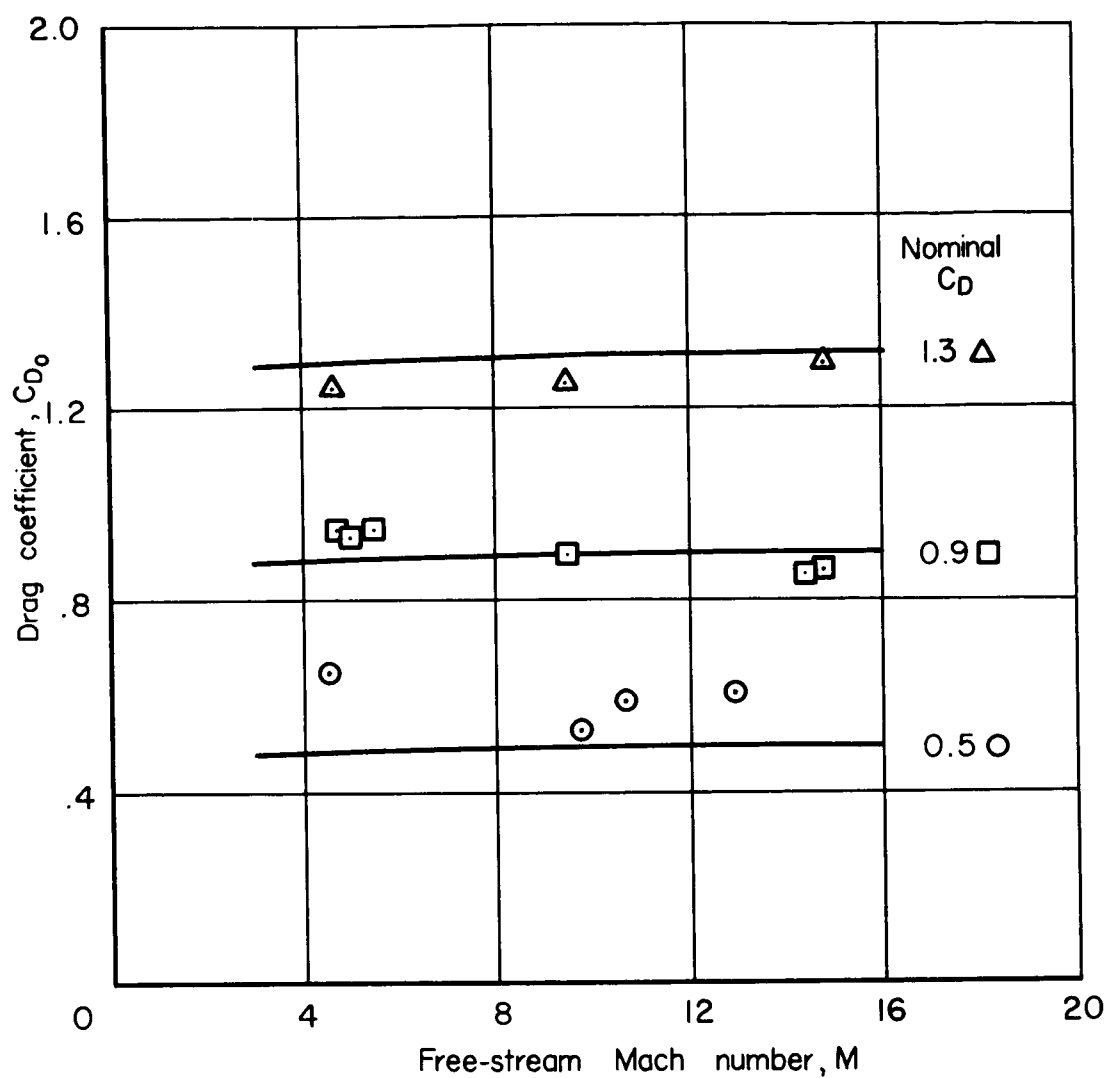
Figure 4.- Drag coefficient vs. Mach number.





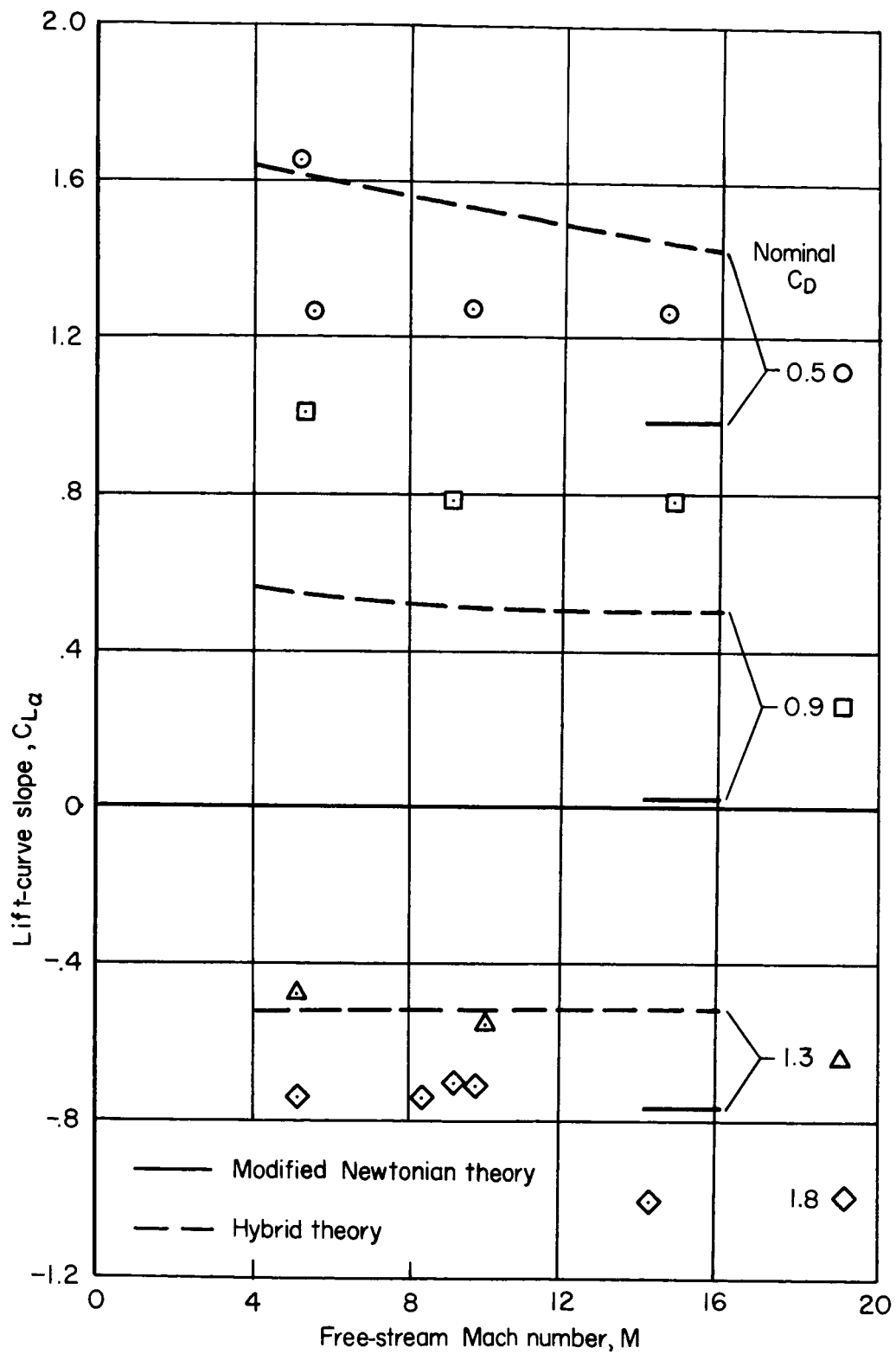
(b) Sphere-cone-cylinder configurations.

Figure 4.- Continued.



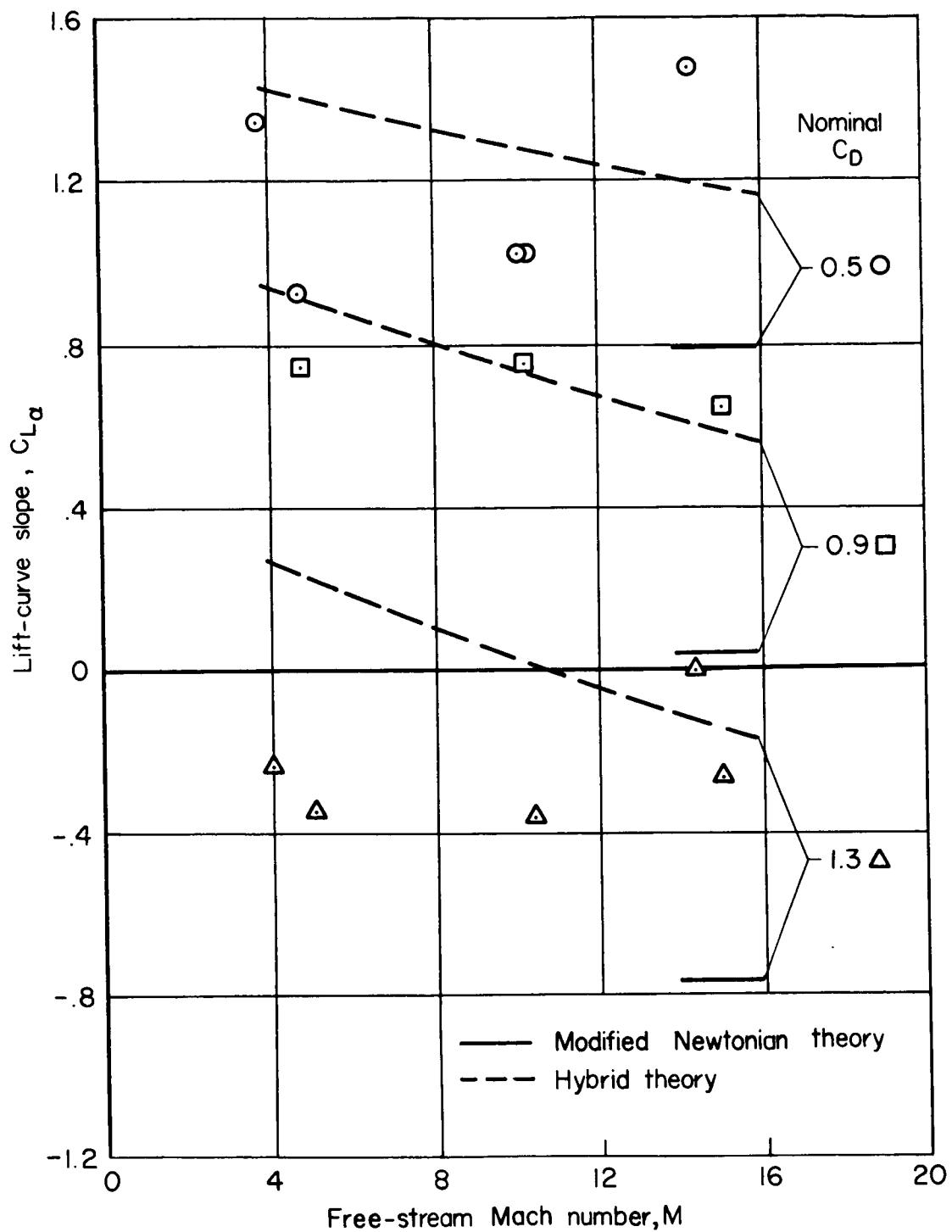
(c) Ellipsoid-cylinder configurations.

Figure 4.- Concluded.



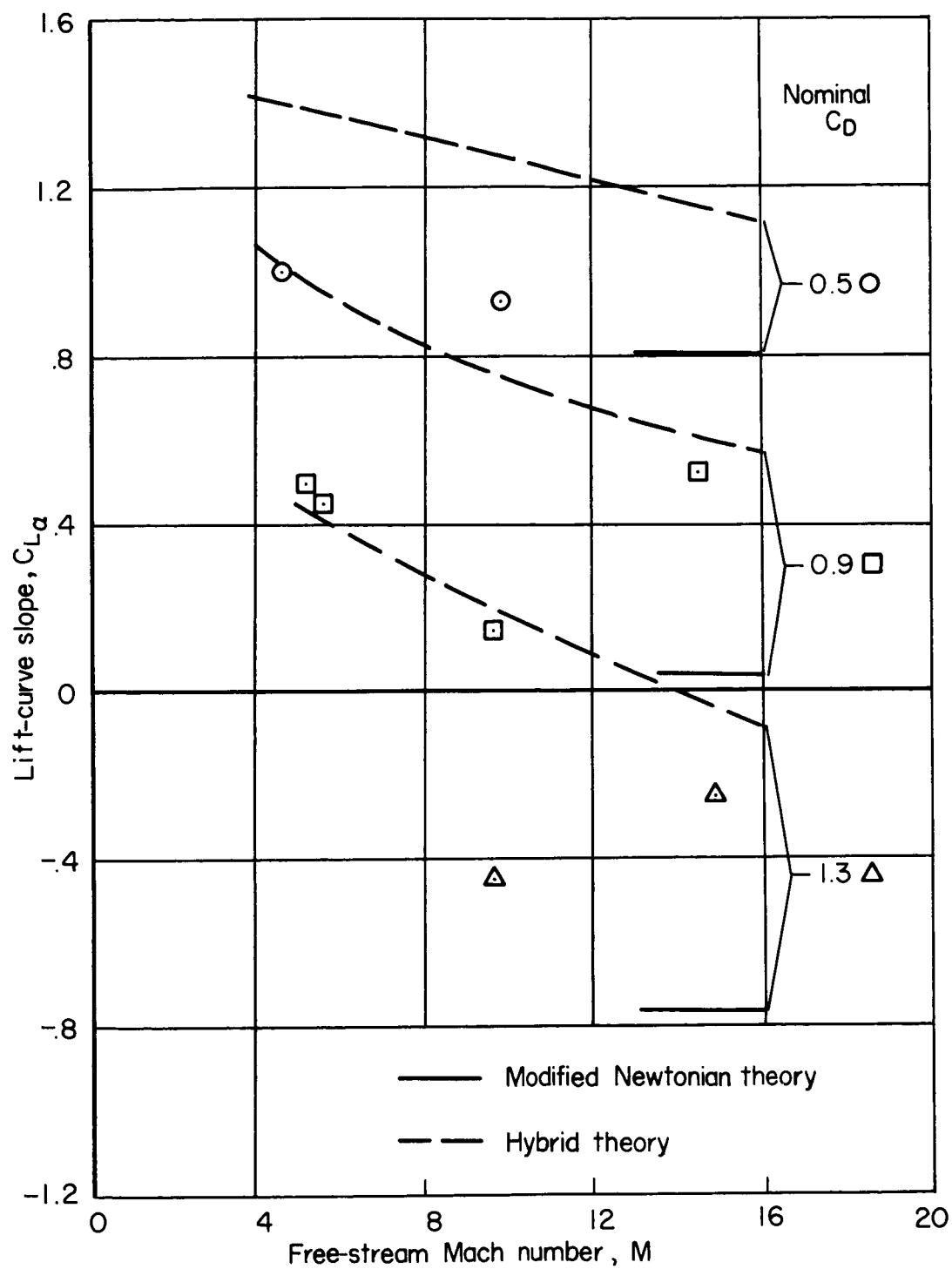
(a) Cone-cylinder configurations.

Figure 5.- Lift curve slope vs. Mach number.



(b) Sphere-cone-cylinder configurations.

Figure 5.- Continued.



(c) Ellipsoid-cylinder configurations.

Figure 5.- Concluded.

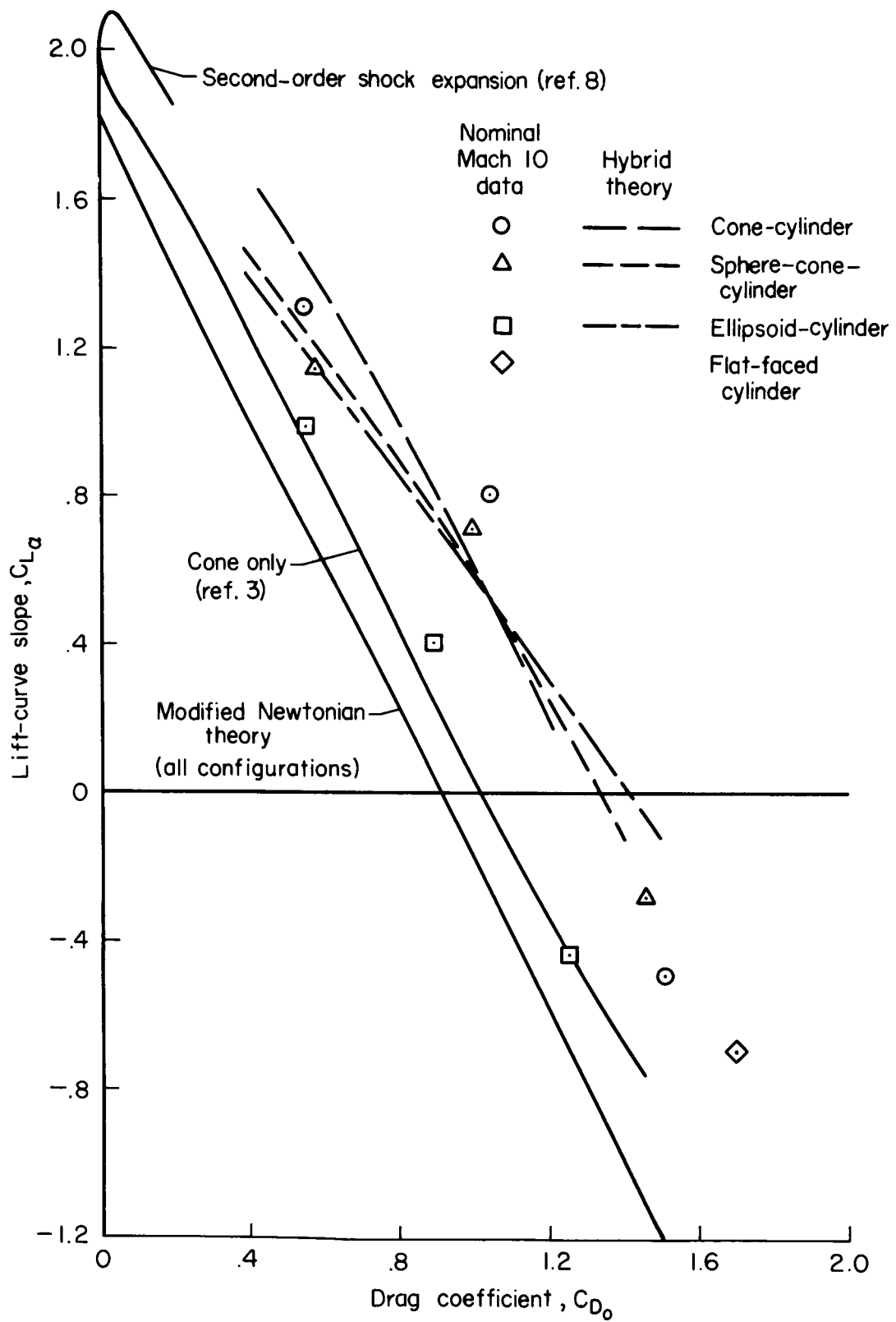
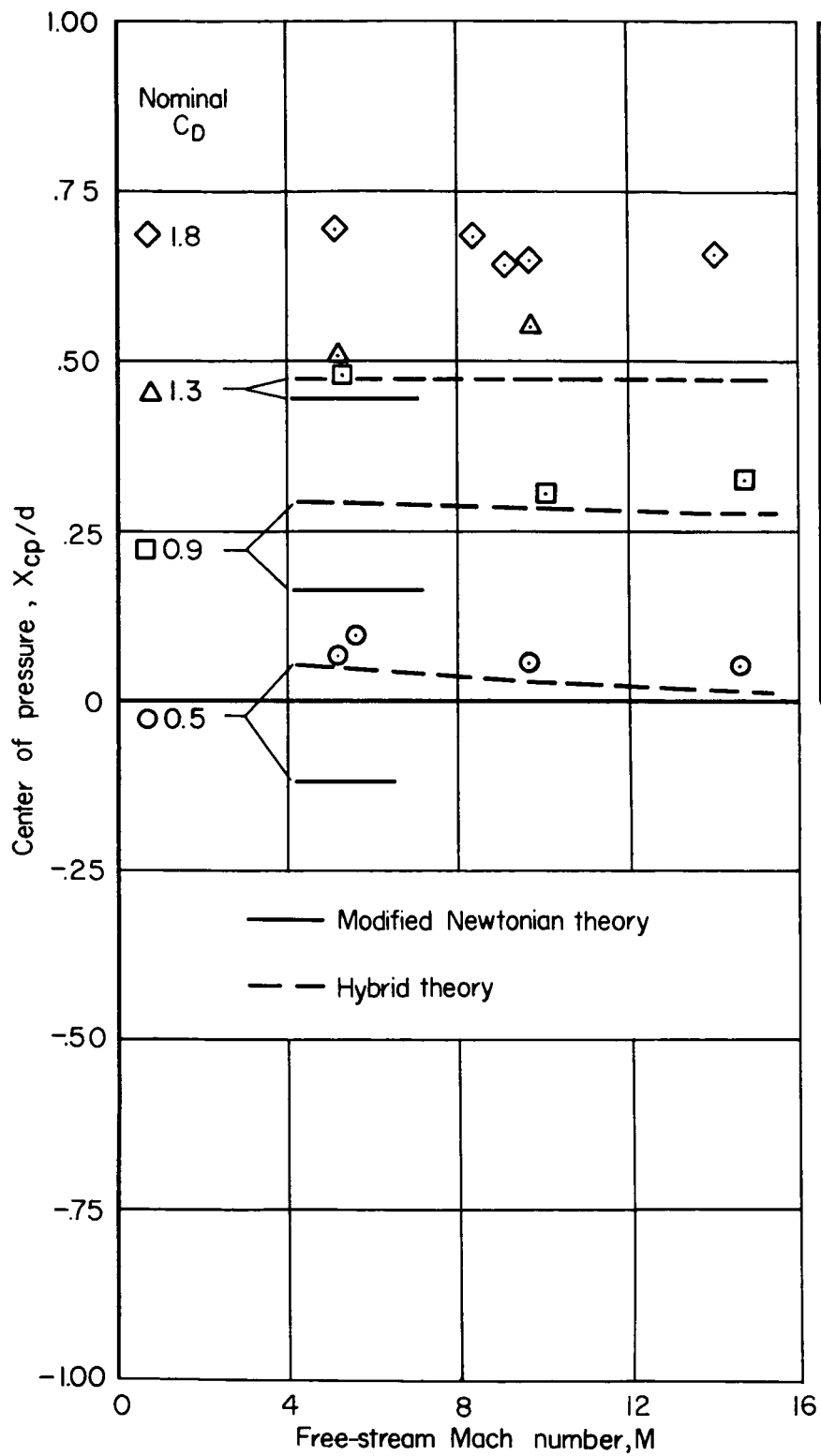
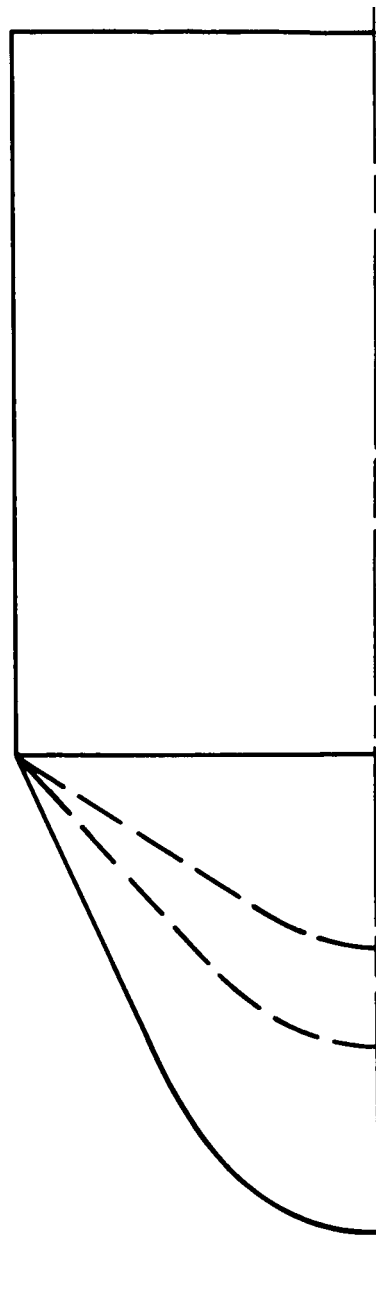
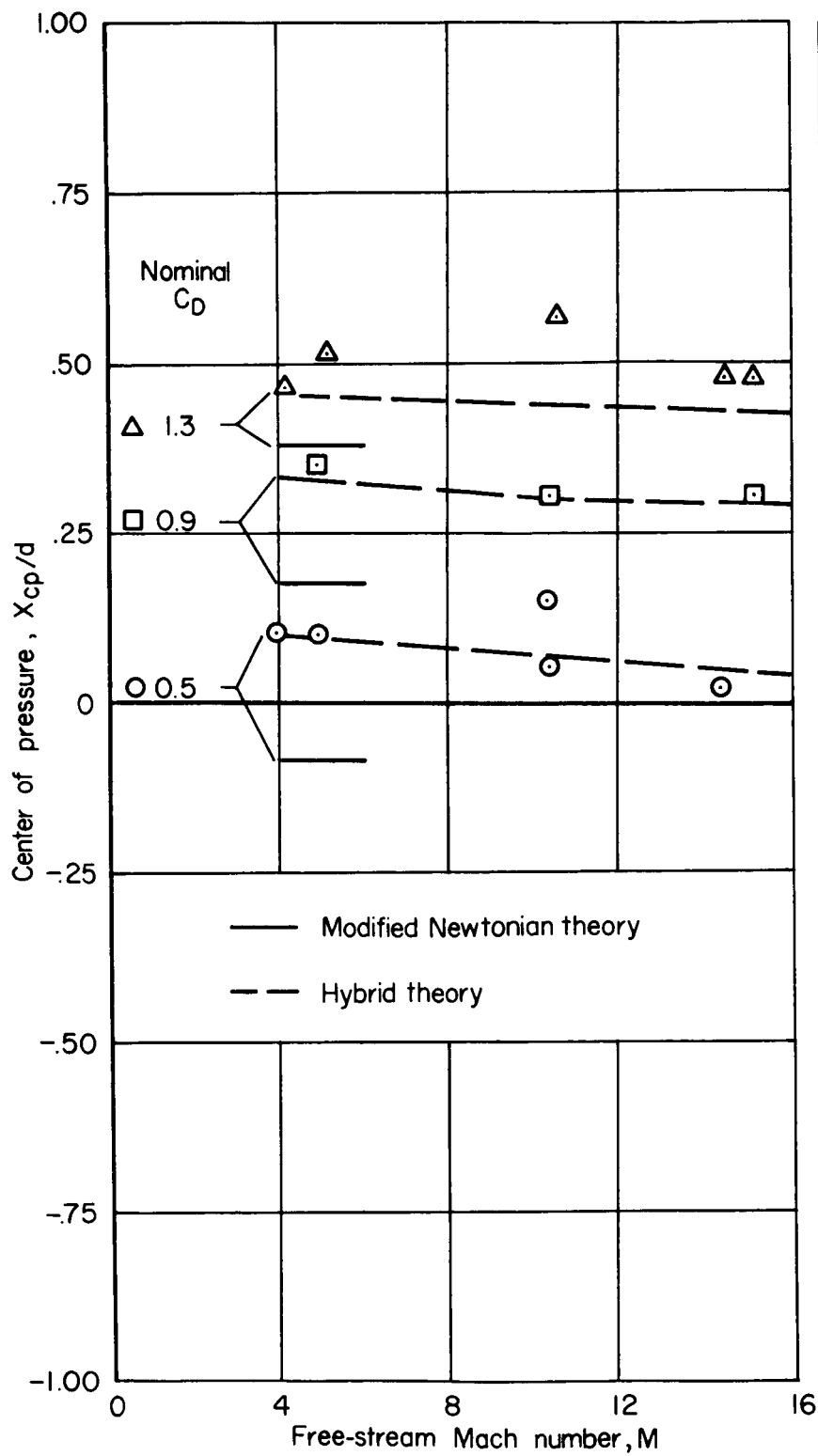


Figure 6.- Lift-drag cross plot.



(a) Cone-cylinder configurations.

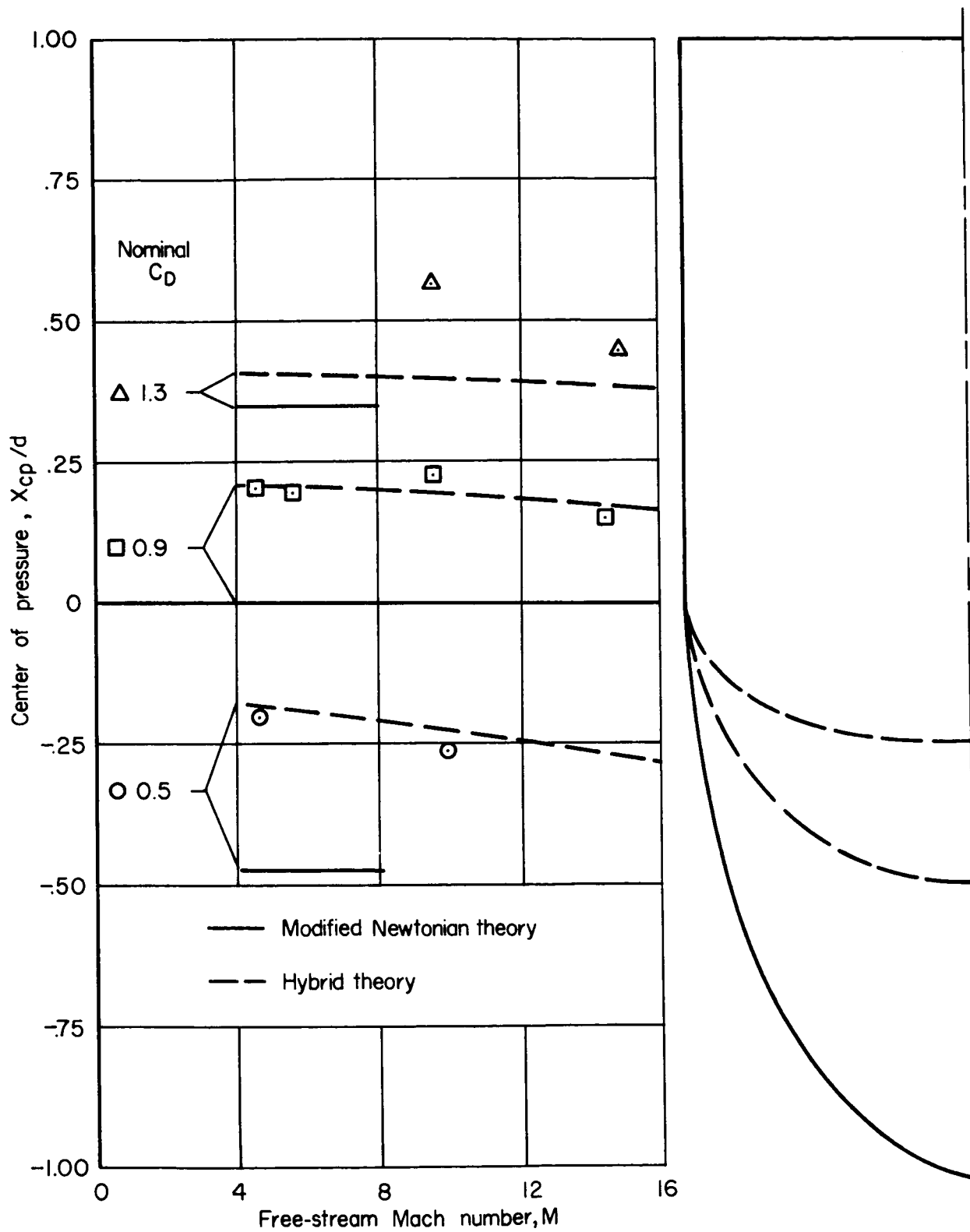
Figure 7.- Center of pressure.



(b) Sphere-cone-cylinder configurations.

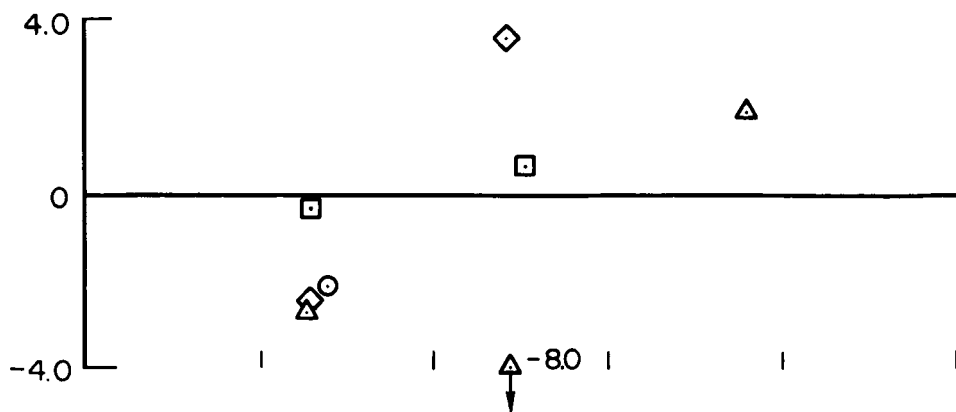
Figure 7.- Continued.





(c) Ellipsoid-cylinder configurations.

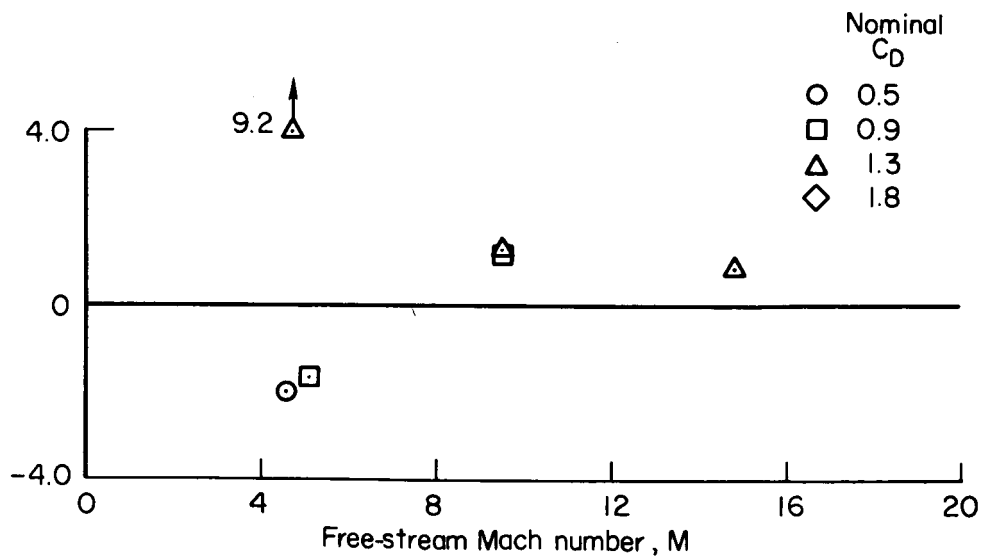
Figure 7.- Concluded.



(a) Cone-cylinder configurations.



(b) Sphere-cone-cylinder configurations.



(c) Ellipsoid-cylinder configurations.

Figure 8.- Dynamic stability.